

Study of PowerFlux Response to Continuous
Wave Signals of Non-Standard Form and
Locations of Potential Sources in the Milky
Way Galaxy

Greg Vansuch, University of Colorado at Boulder
Vladimir Dergachev, Ph.D., California Institute of Technology

September 3, 2011

Abstract

We present results on the robustness of the PowerFlux algorithm to injected signals with various parameters, in particular the speed and period of a gravitational wave, as well as the ability of the algorithm to reconstruct parameters from simulations. We will also describe potential locations of continuous gravitational radiation from various star clusters and the arms of the Milky Way Galaxy.

1 Introduction

Einstein's theory of general relativity predicts the existence of gravitational radiation. A foundation of the theory is that matter curves space-time and that certain changes in the distribution of matter, such as a coalescing binary neutron star system, produce gravitational radiation. This radiation is transverse, meaning that the strain oscillations of gravitational radiation are orthogonal to the direction the radiation propagates, and is also quadrupolar. Gravitational radiation also passes through objects since it is only absorbed, shielded, and scattered to a very small extent [1, 2].

To detect gravitational waves, the Laser Interferometer Gravitational Wave Observatory (LIGO) has two sites for detectors, Hanford, Washington and Livingston, Louisiana. Both sites use an interferometer that is 4 kilometers long [1, 2, 3, 4] with two stainless steel tubes, each with a partially transmissive input mirror and highly reflective end mirror [1, 2, 3, 4]. A visualization of gravitational radiation and the design of the interferometers is provided in Figure 1.

Gravitational radiation that arrives at the detectors will be very weak and will alter the length of the arm by 10^{-18} m or less [1]; however, a gravitational wave has yet to be detected since these waves are very weak and because data gathered from the interferometers is susceptible to noise. This noise includes seismic and thermal noise; quantum vacuum noise; gravity gradient noise; shot noise from the beam; thermal suspension noise; and actuation noise from the electronics [1, 2]. The design of the interferometers is being improved to increase sensitivity.

The sources of gravitational radiation that are strong enough to detect are astrophysical objects; terrestrial sources produce radiation that is far too weak to detect once the detectors receive the signal [4, 5]. Some gravitational waves that are strong enough to detect are present for only a fraction of

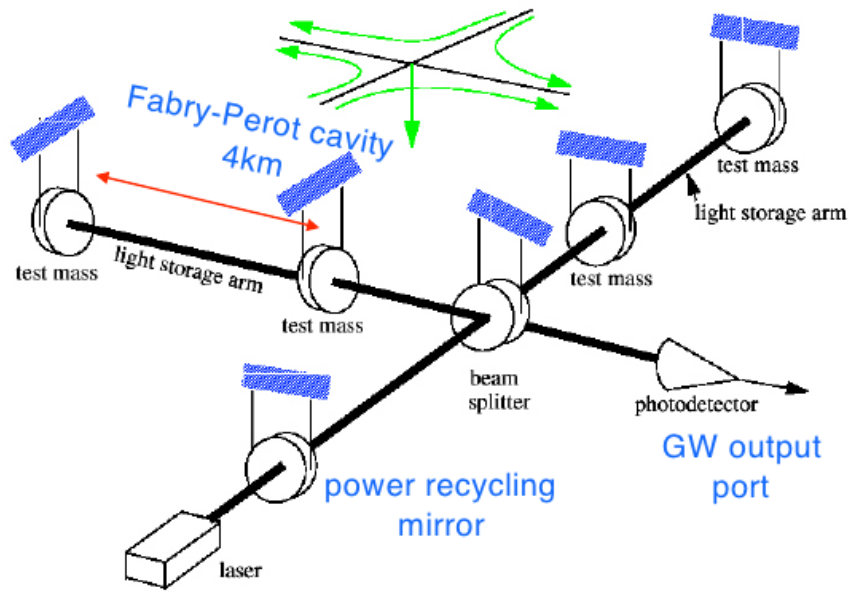


Figure 1: A gravitational wave expands space in one dimension and contracts space in the other dimension due to its quadrupolar nature, represented by the four contracting and expanding green arrows. [1]. The rest of this picture shows the basic design of an interferometer. The laser is shot through a power recycling mirror and then into a beam splitter. It enters the Fabry-Perot cavity where the power of the laser beam is built up. When noise or radiation is present, the light will travel a distance a distance $L \pm \delta L$, where L is the length of the interferometer. The interferometer is sensitive to δL of a fraction of a wavelength of light, allowing for it to be very sensitive to gravitational radiation [1]. Source: [2].

a second while continuous waves are present for extended periods of time. Sources of continuous gravitational radiation are spinning neutron stars that are asymmetrical along the axis of rotation [1, 2, 3, 4]. According to the accepted model of a neutron star emitting continuous gravitational radiation, a star will emit waves with twice its rotational frequency [6, 7].

To search for these waves, the PowerFlux algorithm is utilized. In Section 2, we give a brief overview of this algorithm. In Sections 3 and 4, the results of injections with the algorithm will be discussed. Sections 5 and 6 will introduce two methods to search for neutron stars in the Milky Way Galaxy that may be emitting continuous gravitational waves.

2 PowerFlux: An Overview

The PowerFlux algorithm is a semi-coherent code that computes the power from a particular direction in the sky at a certain frequency and spindown using the weighted sum [5, 8]

$$P[k, f_t, a_t] = \frac{\sum_t (a_t)^2 |z_{t,k+f_t}|^2 / w_t^4}{\sum_t (a_t)^4 / (w_t)^4} \quad (1)$$

The algorithm divides input data into N short portions that have all undergone a Fourier transform and searches for signals with constant amplitudes that are put into frequency bins $\{a_k\}_{k=1}^N$ with varying phases $\{\phi_k\}_{k=1}^N$. Letting the set T be all possible phases in the output data, T forms an N dimensional torus where the power P of a coherent sum is a smooth function defined by the equation [5],

$$P = \left| \sum_{k=1}^N a_k \cdot e^{-i\phi_k} \right|^2 = \sum_{k=1}^N a_k^* a_l \cdot e^{i(\phi_k - \phi_l)} \quad (2)$$

We then define the set S , where S is a subset of T . A group of signals will have certain phase constraints and are located in the submanifold $S \subset T$. To know that a signal from S has been detected, a statistic P is constructed that has a high value in the presence of a signal and a low value when a signal is not present [5]. When it is determined that a signal from S has been detected, S is partitioned into smaller and smaller subsets until the signal is recovered [5].

The semi-coherent method is excellent for searching for signals with large phase evolutions; however, the sensitivity with this method is limited. To

achieve a higher sensitivity, as well as to work around memory problems that were beginning to emerge, small changes were made to the original PowerFlux to create PowerFlux2. These changes included the addition of a partial power sum cache and increased sensitivity (at the sacrifice of computational efficiency that is not as great as the original PowerFlux). The increased sensitivity introduced a loosely coherent method of analysis that searches smaller portions of the sky than the semi-coherent method [5, 8].

3 Analysis of Injections Varying the Speed of Continuous Gravitational Waves

In this section we discuss how a gravitational wave signal will appear in a PowerFlux analysis when the speed of an injected wave is different from the speed of light. To do this, we varied the parameter λ that PowerFlux uses to demodulate the speed of a reconstructed signal from the speed of light.

Before beginning injections that varied the speed of a gravitational wave, PowerFlux installation was verifying using [8]. Afterwards, several parameters of the configuration file from page 50 of [8] were altered: the frequency of the gravitational wave was altered to 500Hz, the first bin was altered to 900000, the iota was altered to 0, the spindown was altered to 0Hz/s, and the strain was altered to 6e-24. The PowerFlux program was run and the signal-to-noise ratio skymap viewed, which is seen in Figure 2.

We then began to vary the speed of gravitational waves in our analysis. To do this, the Doppler-multiplier parameter, λ , is varied. This is a constant that the Doppler shift for demodulation is multiplied by, essentially providing mismatch that is below the speed of the incoming signal and the PowerFlux algorithm signal model [8].

The Doppler-shift is defined by the equation,

$$f' = f \left(1 + \frac{v}{c} \right) \quad (3)$$

where f is the frequency of the injected signal, c the speed of light, f' the frequency of the reconstructed signal, and v is,

$$v = \vec{v}_{\text{earth}} \cdot \vec{e}_{\text{sky position}} \quad (4)$$

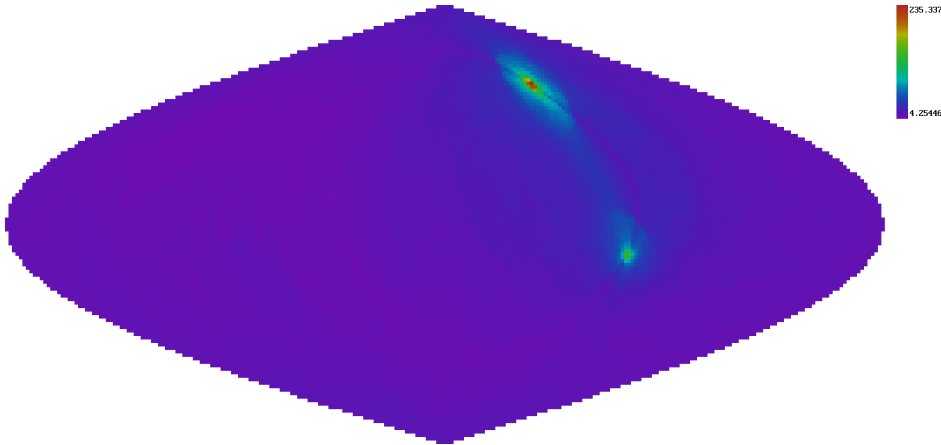


Figure 2: With this injection, the speed of the continuous gravitational wave is assumed to be the speed of light, with the injected signal coming from the location specified by the simulated signal injecting into Gaussian noise of [8], which is right ascension 2.0 and declination 1.0. In this particular skymap, the reconstructed signal is located at the same position, which is clearly seen above the noise with an Signal-to-Noise Ratio (SNR) of ~ 235 .

To find this dot product, we note that, in Ptolemaic approximation, the orbit of the earth is a circle that may be described by,

$$\begin{aligned} x &= R \cos(\Omega t) \\ y &= R \sin(\Omega t) \\ z &= 0 \end{aligned} \tag{5}$$

where the derivatives of these give the velocity of the earth,

$$\begin{aligned} \dot{x} &= -\Omega R \sin(\Omega t) \\ \dot{y} &= \Omega R \cos(\Omega t) \\ \dot{z} &= 0 \end{aligned} \tag{6}$$

We then note that a location in sky may be described by celestial coordinates,

$$\begin{aligned} x &= \cos \theta \cos \varphi \\ y &= \cos \theta \sin \varphi \\ z &= \sin \theta \end{aligned} \tag{7}$$

Thus, we get

$$\begin{aligned}
v &= \vec{v}_{\text{earth}} \cdot \vec{e}_{\text{sky position}} \\
&= (-\Omega R \sin(\Omega t), \Omega R \cos(\Omega t), 0) \cdot (\cos \theta \cos \varphi, \cos \theta \sin \varphi, \sin \theta) \\
&= -\Omega R \cos(\theta) \sin(\varphi + \Omega t)
\end{aligned} \tag{8}$$

Putting this all together, we see that

$$f' = f \left(1 + \frac{-\Omega R \cos(\theta) \sin(\varphi + \Omega t)}{c} \right) \tag{9}$$

It is seen that when a Doppler-multiplier of 1 is used, the position of the reconstructed signal in the sky is the same as the injected signal, which is the case in Figure 2. When a Doppler-multiplier greater than 1 is used, the speed of the gravitational wave is less than speed of light. The result is that the Doppler effect will be larger than when the speed of the gravitational wave is the speed of light. To compensate for this change, the recovered signal moves toward the ecliptic pole where the Doppler shift due to Earth is at its minimum of 0. This causes the recovered signal to appear closer to the ecliptic pole than the injected signal in Figure 2. When a Doppler-multiplier less than 1 is used, the speed of the gravitational wave is altered to be greater than the speed of light. The result is that the Doppler effect will be smaller than when the gravitational wave travels at the speed of light. To compensate for this change, the recovered signal moves away from the ecliptic pole. This causes the recovered signal to appear further away from the ecliptic pole than the injected signal in Figure 2.

This may be viewed by the definition of the dot product,

$$\cos \theta = \frac{v_{\text{earth}} \cdot v_{\text{sky position}}}{\|v_{\text{earth}}\| \|v_{\text{sky position}}\|}. \tag{10}$$

When the Doppler-multiplier, λ , is brought into this,

$$\cos \theta' = \lambda^{-1} \cos \theta \tag{11}$$

The position of the source in terms of theta is smaller (further away from the ecliptic pole), with smaller λ and that the position of the source in terms of theta is larger (closer to the ecliptic pole) with larger λ .

A video was created to show what the signal-to-noise ratio skymaps look like as the speed of the continuous gravitational wave goes from being greater

than the speed of light by a factor of 5 ($\lambda=0.5$) down to the speed of light ($\lambda=1$), and then less than the speed of light by a factor of 10 ($\lambda = 10$). When the video begins, the speed of the gravitational wave has been increased by a factor of 5 and the location of the reconstructed signal is a huge blob of red around around the position of 2π . With the tools that are available, no gravitational wave traveling at this speed would be detected. As the Doppler-multiplier starts to increase, causing the speed of a gravitational wave to decrease, the Doppler-effect becomes larger and the SNR slowly increases and begins to move in the direction of $\pi/2$ (toward the position of the injected signal and the ecliptic pole). The location of the signal becomes more practical to pinpoint and detect.

The SNR peaks at ~ 235 when the Doppler-multiplier is 1. When the Doppler-multiplier is greater than 1, the signal begins to move even closer to the ecliptic pole than the injected signal to compensate for the increased Doppler effect. The SNR slowly decreases to ~ 43 and the signal remains practical to pinpoint and detect.

We are able to conclude that PowerFlux is able to locate signals that travel at non-standard speeds when the speed of a signal is less than the speed of light and when the speed of a signal is somewhat greater than the speed of light. The algorithm responds to signals that travel at non-standard speeds by shifting the location of maximum SNR based on the Doppler effect that corresponds to a particular speed. PowerFlux is unable to locate signals that travel at speeds significantly greater than c because the Doppler shift due to the rotation of the Earth is not sufficient enough for proper reconstruction.

4 Follow-up Searches for Continuous Gravitational Wave Signals

In this section we discuss the robustness of the PowerFlux algorithm to signals of non-standard frequency period modulations and follow-up results that track a potential signal through a process that discards false candidates in actual LIGO data analysis.

Parameters that must be taken into account during a PowerFlux analysis of continuous gravitational radiation are polarization and frequency of a wave and the spindown and sky location of the source. For all of our injections, the sky location of the injected signal is right ascension 2.0 and declination

1.0. The spindown is a linear component of frequency evolution due to the source losing energy over time. The polarization of the gravitational wave in the injections is circular. The data is divided into 7 chunks.

4.1 Analysis of 8 Month Period

The first analysis that we present is an injection with a period of 8 months. To make this injection, three parameters were added to the configuration file that was used to create Figure 2. These parameters are fake-freq-modulation-depth, fake-freq-modulation-freq, and fake-freq-modulation-phase. The fake-freq-modulation-depth parameter was set to 0.005, which simply sets the depth of the injected signal to $5 \cdot 10^{-3}$ Hz. The fake-freq-modulation-freq parameter is a parameter that modulates the frequency by

$$f_m = \frac{1}{x \cdot \text{months} \cdot \frac{\text{days}}{\text{months}} \cdot \frac{\text{hour}}{\text{day}} \cdot \frac{\text{seconds}}{\text{hour}}} \quad (12)$$

Plugging in 8 months as x , it is seen that $f_m = 4.82253086\text{e-}8$ Hz. The fake-freq-modulation-phase parameter gives the phase of the gravitational wave, which was set to $\pi/2$.

After running the injection the signal-to-noise ratio was found to be 153 at a right ascension of 2.0273 and declination of 0.4725. The SNR skymap is seen in Figure 3.

With a signal appearing at this location, we began follow-up runs. Follow-up runs allow for us to determine whether the reconstructed signal from Figure 3 is a real signal or a detector artifact that presented itself as a candidate. First, we ran an initial follow-up with the loosely-coherent method with a focus right ascension and declination on where a potential signal has presented itself and continue this until we find a focus right ascension and declination where the signal-to-noise ratio is highest. Afterwards, we explored two different follow-up methods. The first introduces the parameter ‘split-ifos’ and the second uses the semi-coherent method, both of which are explained shortly. This followup procedure is summarized in the flowchart in Figure 4.

The initial follow-up run to the signal if Figure 3 had a focus-right ascension and focus-declination were set to where the signal presented itself: RA= 2.027399 and DEC= 0.472589. This follow-up uses the loosely coherent approach. A phase mismatch, which specifies the maximum phase mismatch

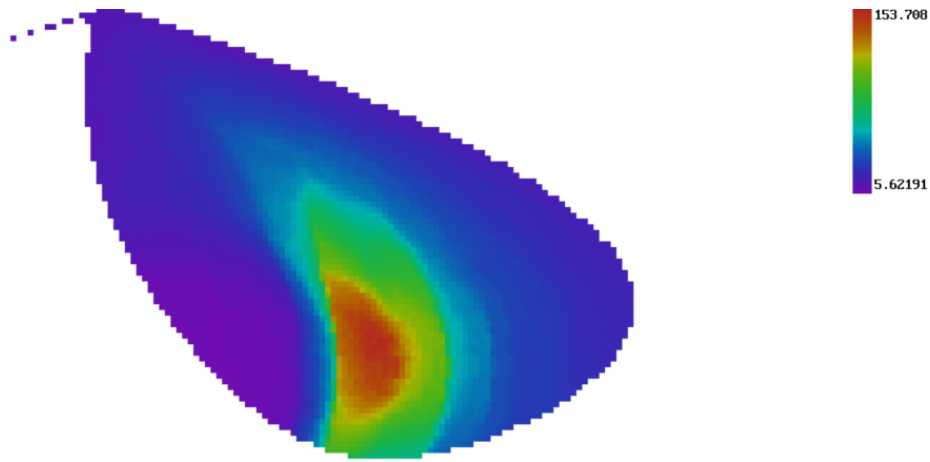


Figure 3: SNR skymap of the 8 month frequency period modulation analysis. The signal appears at RA= 2.0273 and DEC= 0.4725 with an SNR of 153.

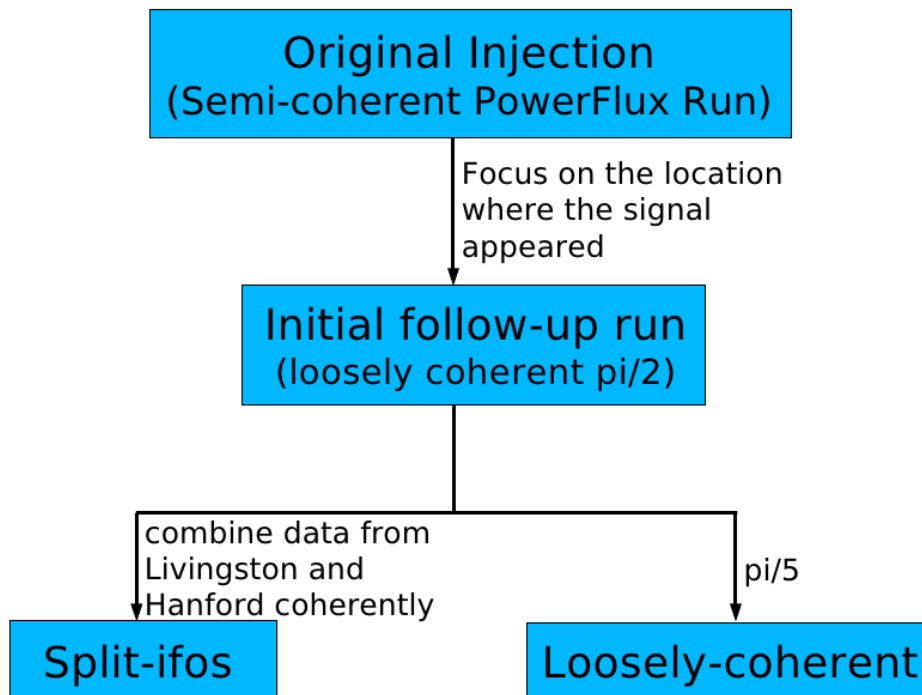


Figure 4: Follow-up method flowchart.

of the coherence length in a loosely-coherent run, [8] of $\pi/2$ was used. When the injection was run, the skymap in Figure 5 was produced.

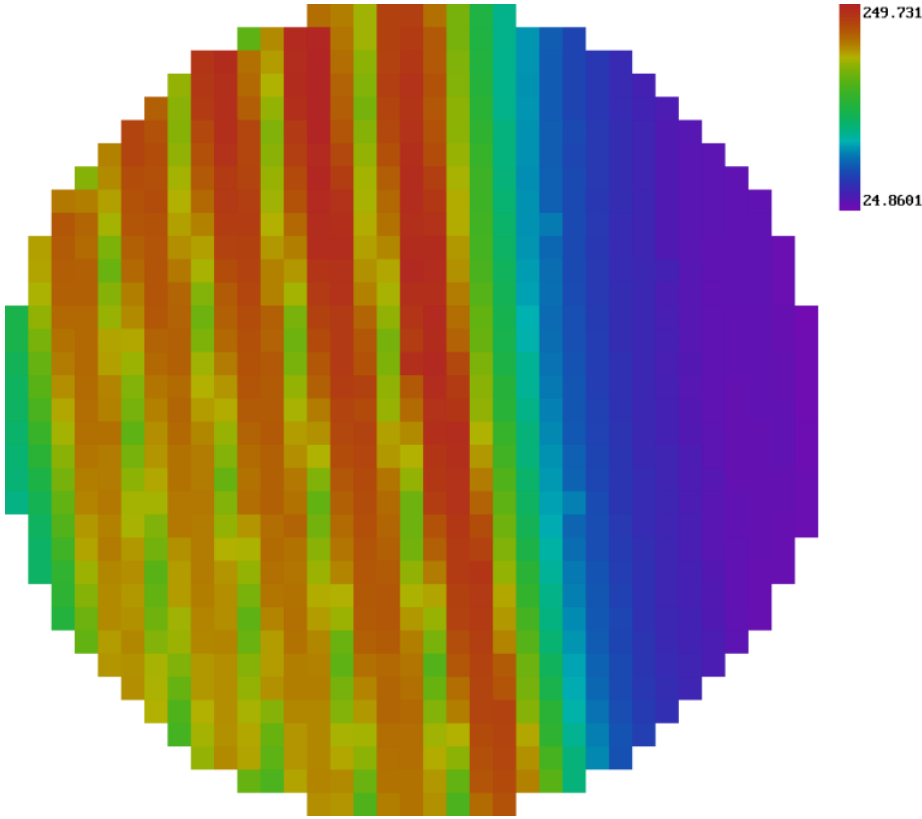


Figure 5: SNR skymap of the 8 month frequency period modulation period analysis initial followup. The signal appears at RA= 2.0578 and DEC= 0.5606 with an SNR of 249 when data chunks 1 to 3 are used. This is below the location of the injected signal and slightly to the left of the injected signal. On this skymap, the signal is essentially in the middle, indicated by very dark red. The spindown that allowed for the signal to be located at this position was $8e-10$.

The signal was able to be reconstructed during this original follow-up, and the spindown of the source was seen to be $8e-10$, which was used in subsequent follow-up runs of this injection. The next step was to see what would occur during the ‘split-ifos’ and semi-coherent method follow-up.

The ‘split-ifos’ parameter is set to a default of ‘1’ where it analyzes a signal at both the Hanford and Livingston interferometer separately. It then adds the results up of both the Hanford and Livingston analysis. In this follow-up,

‘split-ifos’ was set to 0, which coherently combines data from Livingston and Hanford. The skymap may be seen below in Figure 6.

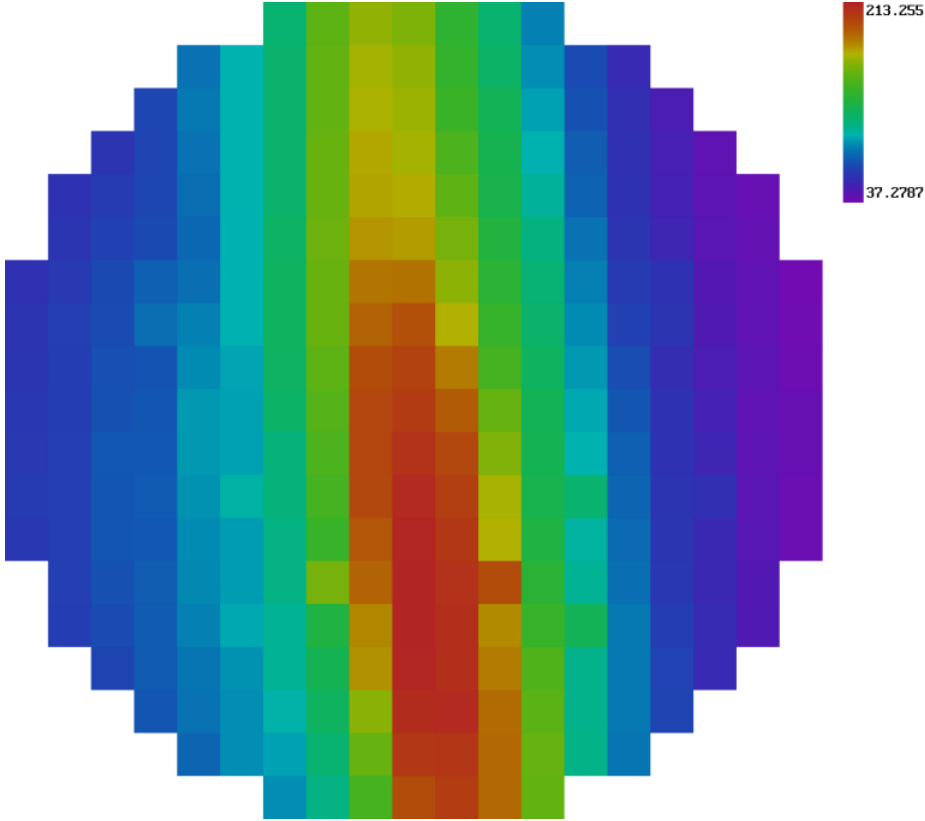


Figure 6: SNR skymap of the 8 month frequency period modulation analysis ‘split-ifos’ followup. The signal appears at RA=2.057842 and DEC= 0.538423 with an SNR of 213.255402 when data chunks 1 to 3 are used.

A ‘split-ifos’ follow-up centered at the location the signal was found in Figure 5 was run, but the SNR was found to be 213 at the same location, indicating that the highest SNR had in fact already been found.

The loosely coherent follow-up uses a much smaller phase mismatch of $\pi/5$ and analyzes the data chunks from LHO and LLO separately and adds the analysis together afterwards. The skymap is seen in Figure 7.

A data table that shows this information is presented in Table 1. An explanation of why the maximum SNR is attained when particular data chunks are analyzed is presented in section 4.3.

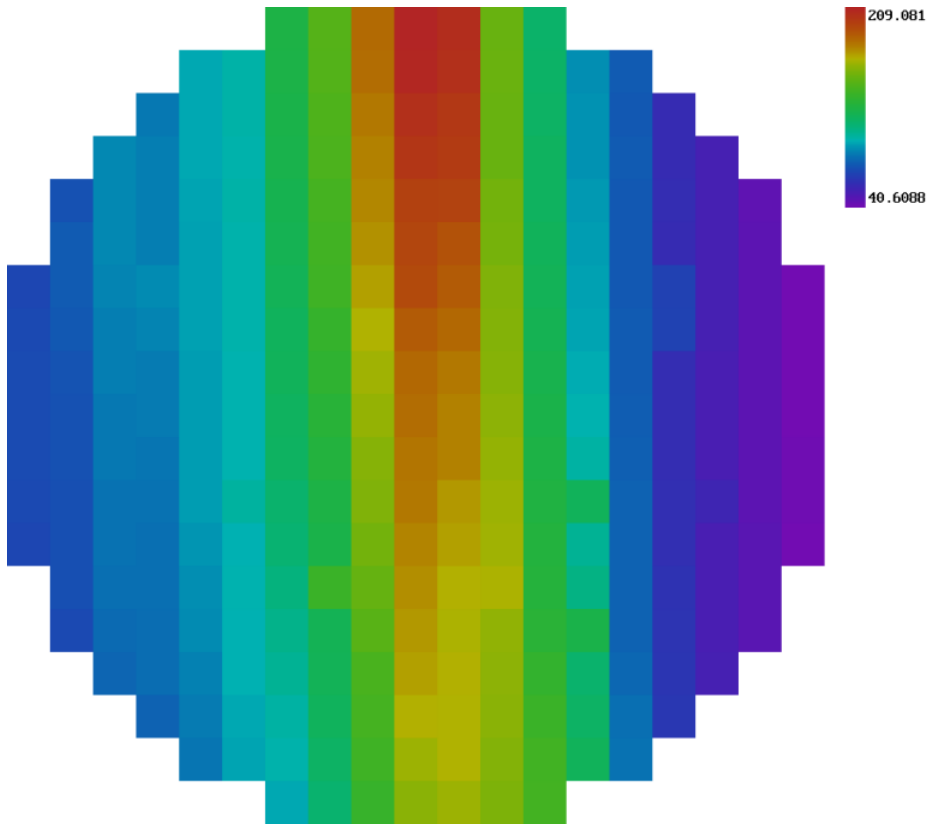


Figure 7: SNR skymap of the 8 month frequency period modulation analysis follow-up using the loosely coherent search. It is clearly seen that the highest SNR on this map is located at the very top, indicating some signal may have been lost due to where this injection was focused. A loosely coherent follow-up with a focus on the locations the highest SNR occurred in this map will occur to find more signal. The data chunks used to find the signal were 2 to 3.

| Type of Run | Maximum SNR | Frequency | RA | DEC | Spindown | Data Chunks |
|--------------------|-------------|-----------|--------|--------|--------------------|-------------|
| Original Injection | 153 | 500.101 | 2.0273 | 0.4725 | $6 \cdot 10^{-10}$ | 0 – 3 |
| Initial Followup | 249 | 500.100 | 2.0578 | 0.5606 | $8 \cdot 10^{-10}$ | 1 – 3 |
| Loosely Coherent | 209 | 500.099 | 2.0551 | 0.6095 | $8 \cdot 10^{-10}$ | 2 – 3 |
| Split-ifos | 213 | 500.100 | 2.0578 | 0.5384 | $8 \cdot 10^{-10}$ | 1 – 3 |

Table 1: It is seen that after the original injection the signal-to-noise ratio increases, and decreases slightly in the loosely coherent and split-ifos followup. The frequency of the signal stays relatively constant, the spindown is constant for the followups, and the data chunks that are used to attain the maximum SNR are within data chunks 0 to 3.

4.2 Analysis of 16 Month Period

The second analysis that we present uses a period of 16 months. The skymap of the original injection is given in Figure 8.

The initial followup was run with the focus-right ascension and focus-declination set to where the signal presented itself in Figure 8. The resulting skymap may be seen in Figure 9.

The 'split-ifos' follow-up was run with the focus location as the location where highest SNR was found in Figure 8, but this time it was run with three different spindowns: 0, $1e-10$, and $-1e-10$. The highest SNR occurred when the spindown was $1e-10$ at right ascension 2.100104 and declination 0.976399 with an SNR of 426.671783 when data chunks 2 to 6 were used in the analysis. The skymap may be seen below in Figure 10.

The loosely coherent follow-up was run and produced the skymap seen in Figure 11.

A data table that shows this information is presented in Table 2.

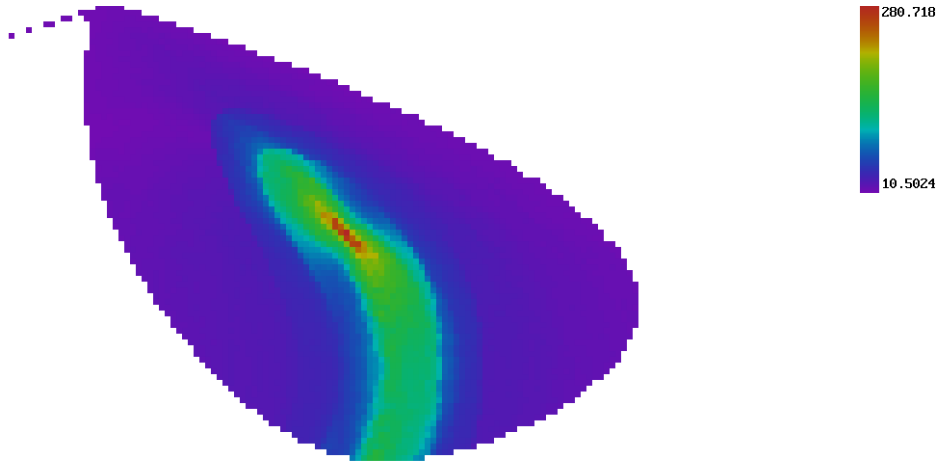


Figure 8: SNR skymap of the 16 month frequency period modulation analysis original injection. The signal is located at RA= 2.102171 and DEC= 0.950848.

| Type of Run | Maximum SNR | Frequency | RA | DEC | Spindown | Data Chunks |
|--------------------|-------------|-----------|--------|--------|--------------------|-------------|
| Original Injection | 280 | 500.098 | 2.1021 | 0.9508 | 0 | 0 – 6 |
| Initial Followup | 566 | 500.098 | 2.0981 | 0.9508 | 0 | 0 – 6 |
| Loosely Coherent | 767 | 500.098 | 2.0962 | 0.9541 | 0 | 1 – 6 |
| Split-ifos | 426 | 500.096 | 2.1001 | 0.9763 | $1 \cdot 10^{-10}$ | 2 – 6 |

Table 2: It is seen that after the original injection the signal-to-noise ratio increases, and decreases slightly in the loosely coherent and split-ifos followup. The frequency of the signal stays relatively constant, the spindown is constant for the followups, and the data chunks that are used to attain the maximum SNR are within data chunks 0 to 6.

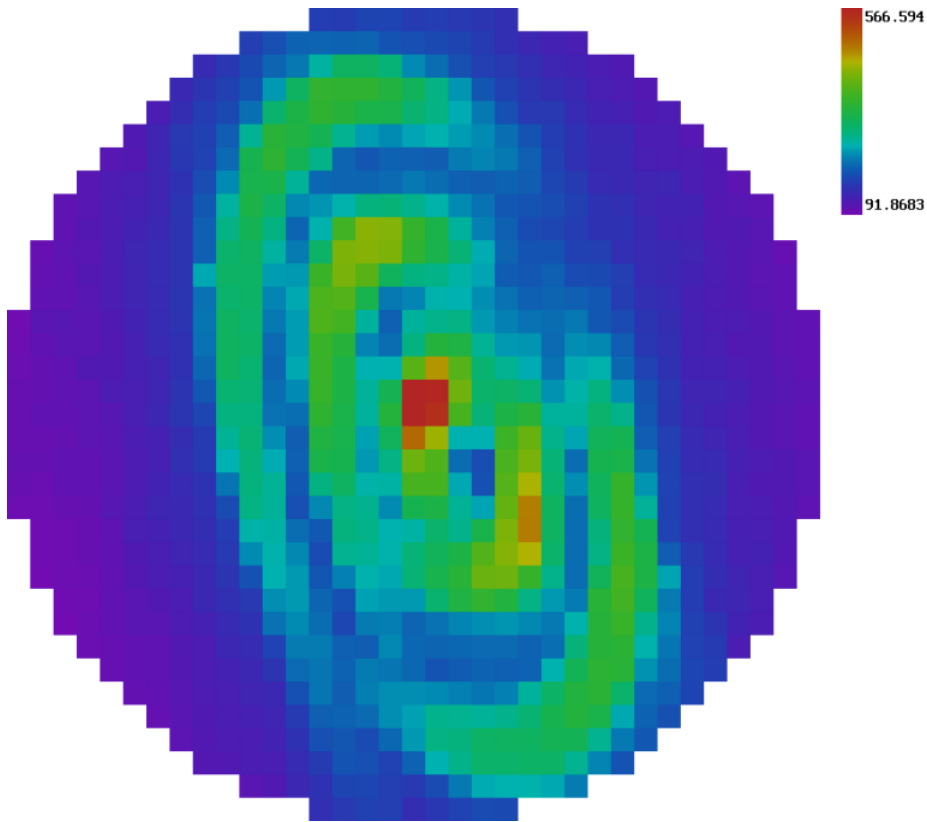


Figure 9: SNR skymap of the initial followup run to the 16 month frequency period modulation analysis. The signal is clearly located in the center at RA= 2.0981 and DEC= 0.8956 with an SNR of 566.

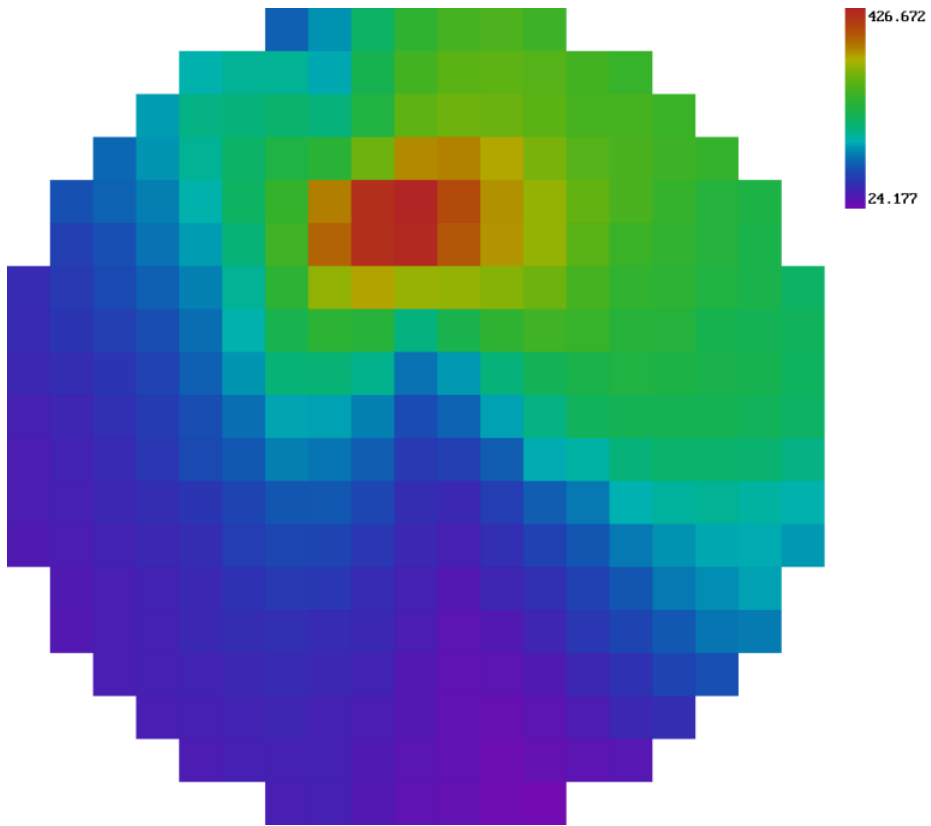


Figure 10: SNR skymap of the 16 month period analysis 'split-ifos' followup at spindown $1e-10$. The SNR of peaked at 426 at a right ascension of 2.1000 and a declination of 0.9763.

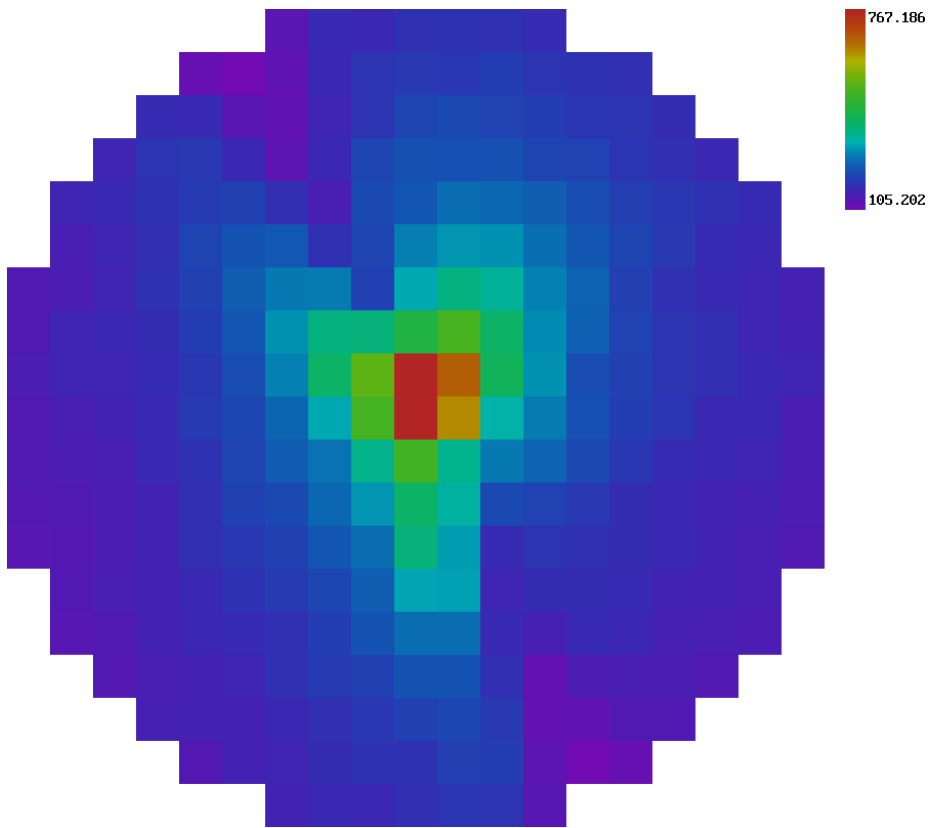


Figure 11: SNR skymap of the 16 month period analysis loosely-coherent followup at spindown 0. The SNR is 767 at right ascension 2.096 and declination 0.9541, with data chunks 1 to 6 used in the analysis.

4.3 Analysis and Conclusions

We will now discuss the reason the maximum signal-to-noise ratio is typically found with data chunks 1 to 3 for the 8 month frequency period modulation and in general with data chunks 0 to 6 for the 16 month frequency period modulation.

The form of our gravitational wave is

$$f = A \sin(2\pi f_m t + \phi) \quad (13)$$

where A is the depth of the gravitational wave, f_m is the frequency modulation of the gravitational wave, and t is the period of the gravitational wave, and ϕ is the phase of the wave.

For the 8 month period modulation, the period is 8 months, the frequency modulation, in months, is 0.125 1/months, the depth in our injections is $5 \cdot 10^{-3}$ Hz, the phase in the injection is $\pi/5$, and the time is 8 months. Since we used 7 data chunks, we may plot the form of our gravitational wave and divide it into the 7 data chunks that were used. This plot is seen in Figure 12. On this plot we have included the signal to noise ratio of the original injection and followup runs and have also indicated the data chunks analyzed by PowerFlux to attain the maximum SNR.

It is seen that the more cubic portion of the curve in Figure 12 occurs from data chunks 1 to 3 and 3 to 5. Since PowerFlux subtracts out a linear term during its analysis, the cubic portion allows for more signal to be extracted over the noise. Thus, we should theoretically find the maximum signal to noise ratio over this cubic portion of the curve. As indicated by the markings of which data chunks were used to attain the maximum signal-to-noise ratio for the original injection and the followup runs, the maximum SNR was found over the cubic portion that includes data chunks 1 to 3. Our results were consistent with theory, where data chunks 1 to 3 were more favored than data chunks 3 to 5. It is rather surprising that only data chunks 2 to 3 were used to attain the maximum SNR for the loosely coherent followup and it is believed that either the injection was run incorrectly or an aspect is being overlooked in how to explain why such little data would be used to attain this SNR.

For the 16 month period modulation, all the parameters are the same except that the frequency modulation is (1/16 months). We plotted the curve (Figure 13) and included the signal to noise ratio of the original injection and

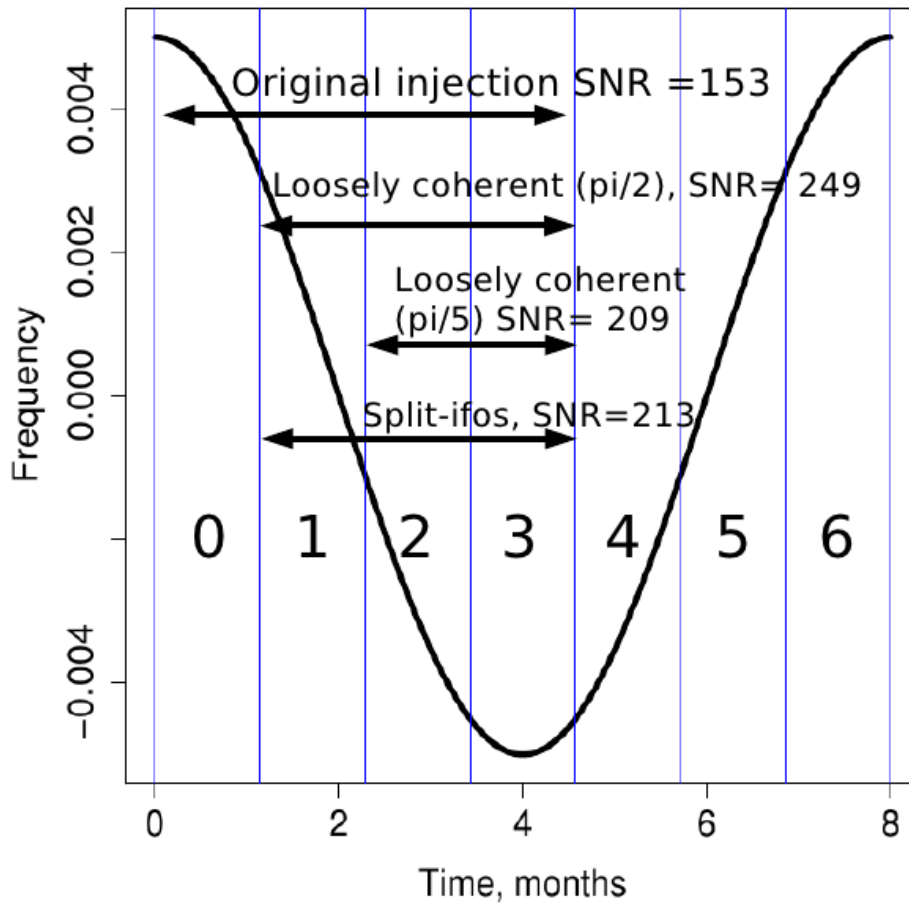


Figure 12: 8 month frequency period modulation plot of frequency vs. time. The data chunks are indicated by the lines and marked 0,1,..6.

followup runs and have also indicated the data chunks analyzed by PowerFlux to attain the maximum SNR.

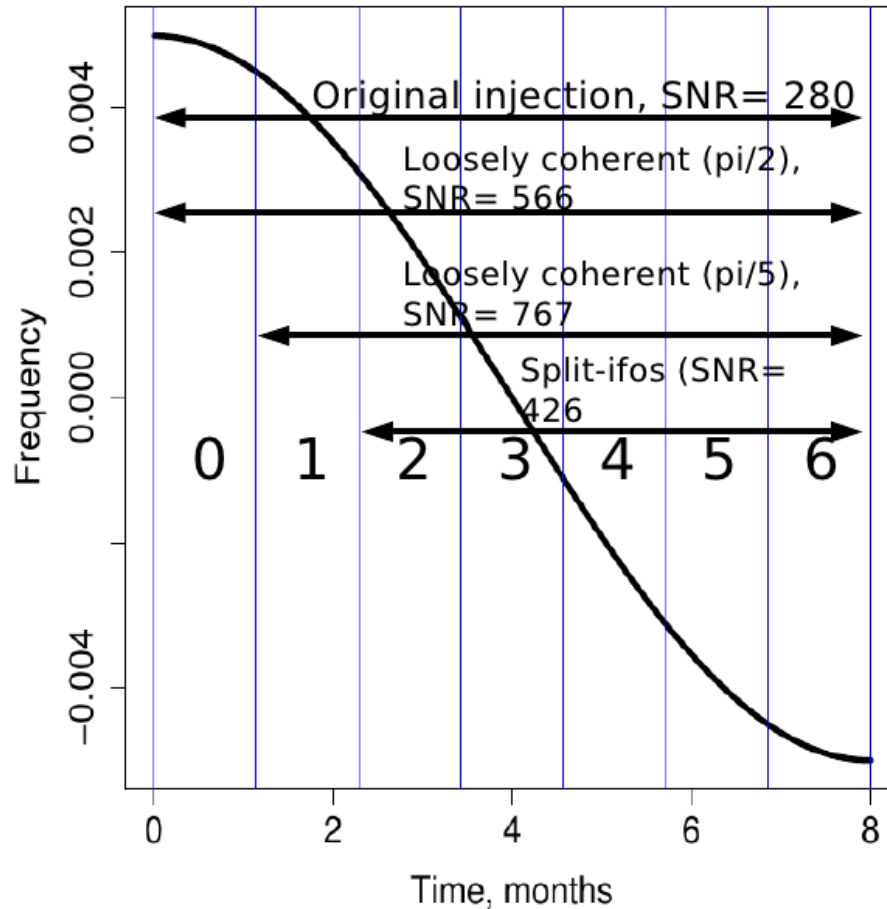


Figure 13: 8 month frequency period modulation plot of frequency vs. time.

It is seen that the more cubic portion of this curve occurs from data chunks 1 to 5 and that, theoretically, the maximum signal to noise ratio will be found over this portion of the curve. As indicated by the markings of the data chunks that were used to attain the maximum signal-to-noise ratio for the original injection and the followup runs, this theory held and, in fact, more data was used to attain the maximum SNR in all cases.

We are able to conclude that PowerFlux was able to follow the signals correctly for both an 8 month and 16 month frequency period modulation and

that the maximum SNR is attained within the region it should theoretically be located. In some cases, even more data is used to attain this maximum signal-to-noise ratio than theory suggests, showing that PowerFlux responds to the modulation of the frequency’s phase beyond what is expected.

4.4 Looking at S6 Data

This section presents the followup of a potential signal from the LIGO S6 data run. Recently, PowerFlux ran a code on the S6 data to detect potential outliers. When the results returned, we began follow up runs on some of these outliers. One of the outliers was outlier 104. We ran an initial followup on it and attained a signal to noise ratio of 8.606 with a spindown of $6.6 \cdot 10^{-9}$ when data chunks 0-6 were analyzed. The skymap may be seen in Figure 14.

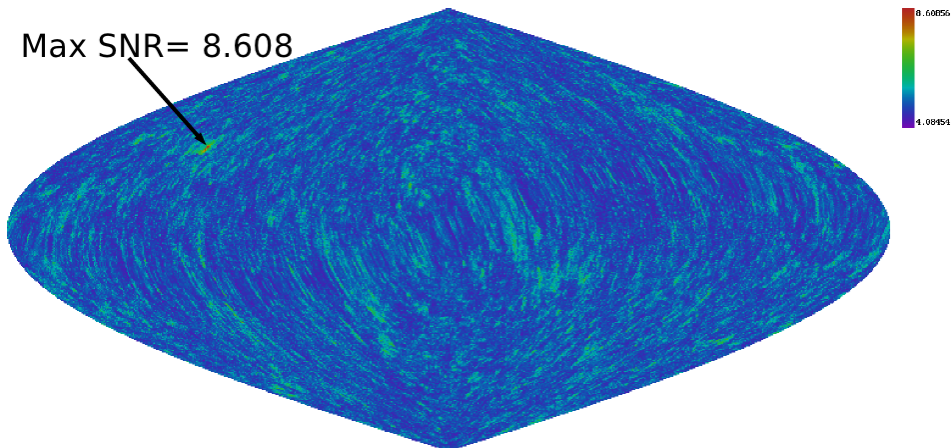


Figure 14: Skymap of the initial followup of outlier 104.

The signal-to-noise ratio was determined to be high enough to run the loosely coherent and the split-ifos followup. The results of all three followup runs are presented below in Table 3.

It is seen that the spindown, frequency and data chunks used to attain the maximum SNR stayed relatively constant and that the potential signal did not move much during the followup runs as indicated by the right ascension and declination values. The loosely coherent method had increased the SNR quite a bit and, while the SNR in the split-ifos followup had gone decreased

| Type | Maximum SNR | RA | DEC | Spindown | Frequency | Data Chunks |
|------------------|-------------|--------|--------|---------------------|-----------|-------------|
| Initial Followup | 8.608 | 5.1988 | 0.5730 | $6.6 \cdot 10^{-9}$ | 1441.301 | 0 – 6 |
| Loosely Coherent | 8.832 | 5.1561 | 0.5738 | $6.5 \cdot 10^{-9}$ | 1441.301 | 1 – 5 |
| Split-ifos | 8.262 | 5.1924 | 0.5692 | $6.5 \cdot 10^{-9}$ | 1441.301 | 0 – 6 |

Table 3: Followup results of outlier 104.

in comparison to the other two followups, the SNR was still rather high. Despite the fact that this looked like a potential signal, it was ruled out as the 60 Hz harmonic since the frequency of the outlier is right by this harmonic, as $24 \cdot 60 \text{ Hz} = 1440 \text{ Hz}$, which is very close to 1441.301 Hz

Other outliers were followed up, all of which were ruled out as well.

5 Potential Locations of Astrophysical Sources of Gravitational Waves

Astronomers have already documented many potential sources of continuous gravitational waves; however, there are many sources that astronomers are not able to locate by conventional methods. To search for these locations, the ATNF [14] database (to understand distributions of known pulsars) and the WEBDA [9] databases were used. The ATNF database contains information on pulsars. What we did was generate a chart [10] of the number of pulsars with frequencies greater than 10Hz, 50Hz, 100Hz, 200Hz, and 500Hz that are distances less than 500pc, 1000pc, 2000pc, 5000pc, and 10000pc from Earth (see Table 4).

Following this, a histogram (Figure 15) was created that shows the angular distance of the pulsars from the center of the galaxy. The center of the galaxy is Sagittarius A* which has a right ascension of 17h 45m 40.045s and a declination of -29 0 27.9. The angular distance between any two points in it is mathematically related by

$$d_{sph} = a \cos(\sin(DEC) \cdot \sin(DEC_{S_a}) + \cos(DEC) \cdot \cos(DEC_{S_a}) \cdot \cos(RA - RA_{S_a})) \quad (14)$$

where sph is the the angular distance, DEC and RA the declination and right ascension of the pulsar, respectively, and DEC SA and RA SA the declination and right ascension of the center of the galaxy.

| Range | F10 | F50 | F100 | F299 | F500 |
|---------|-----|-----|------|------|------|
| 500pc | 9 | 8 | 8 | 6 | 0 |
| 1000pc | 33 | 28 | 25 | 15 | 2 |
| 2000pc | 82 | 68 | 64 | 43 | 5 |
| 5000pc | 115 | 114 | 106 | 78 | 5 |
| 10000pc | 250 | 192 | 177 | 126 | 9 |

Table 4: ATNF [14] data; shows the amount of pulsars with frequencies greater than 10Hz, 50Hz, 100Hz, 200Hz, and 500Hz that are distances less than 500pc, 1000pc, 2000pc, 5000pc, and 10000pc from Earth. Made with [10].

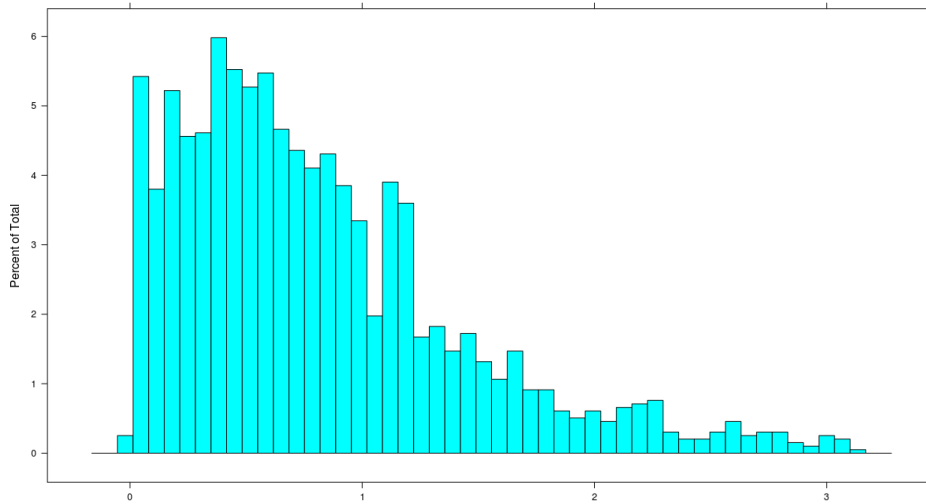


Figure 15: Shows the the percentage of the pulsars from the ATNF [14] database that have an angular distance of 0-0.3 radians from the center of the Milky Way Galaxy. There was a rapid increase in the amount of pulsars present at an angular distance less than 0.1 radians. Made with [10].

| Range | D1 | D5 | D10 | D15 | D30 | D100 |
|---------|-----|-----|-----|-----|------|------|
| 500pc | 0 | 7 | 26 | 49 | 69 | 90 |
| 1000pc | 9 | 93 | 206 | 266 | 317 | 340 |
| 2000pc | 41 | 335 | 521 | 601 | 658 | 681 |
| 5000pc | 123 | 610 | 839 | 924 | 981 | 1004 |
| 10000pc | 148 | 657 | 890 | 975 | 1032 | 1055 |

Table 5: D1 is .01 arcminutes, D5 is .05 arcminutes; this table uses WEBDA [9] data and shows how many clusters there are within certain arc minutes and parsecs from Earth. Made with [10].

We investigated why there was a rapid increase in the amount of pulsars at an angular distance less than 0.1 radians. Using the R program [10], we looked at how many pulsars there were within 0.05 radians and increased this value by 0.01 until the rapid increase was seen. This occurred with an angular distance of 0.08 radians. The reason for this is that the Terzan 5 cluster, which contains many pulsars [15], is an angular distance of 0.08 radians from the center of the Milky Way Galaxy. It is 5.5 ± 0.9 kpc from the Earth.

The Terzan 5 cluster is too far away for us to search for potential astrophysical sources of continuous gravitational waves using PowerFlux. The clusters and pulsars need to be within about 1 kpc or less. Information was gathered from the WEBDA [9] database, which has information on the thousands of clusters that have been observed. Since the cluster locations are given in terms of declination and right ascension, a code was written to determine how many of the clusters that are within a disk of a certain radius in parsecs [10]. This was made into a chart (see Table 5).

The clusters that would be interesting to a PowerFlux search are those within about 1000pc that contain many stars (so that there is a high probability for a pulsar emitting continuous gravitational waves to be present). One of these clusters is Melotte 2, better known as Pleiadas, which is about 120-140 pc from the Sun and contains a few thousand stars and may have pulsars that have yet to be found due to astrophysical phenomena that makes it difficult to see parts of the cluster.

NGC 1999 and NGC 1977 (also known as the “Running Man” Nebula) were also found. NGC 1999, which was found using [12] instead of with

the webda search using [10], is located at a distance of about 430 pc from the Sun in a region of the Milky Way of active star formation, which is a sign that there may be a neutron star emitting continuous gravitational waves. Located in it is a “Bok globule” which is a black spot that is so dense it completely obscures stars behind it [11]. This means that we have no idea what may be located in this region. Combined with the fact it is in an active star forming region, we have reason to search its location for neutron stars that are potentially emitting continuous gravitational waves.

NGC 1977 is at a distance of about 499 pc from the Sun and is close to NGC 1977, which raises an interest in looking for sources of continuous gravitational waves in its region as well.

Other regions that may be worth further investigation to determine if it is worth searching for neutron stars emitting CWs would be the Southern Pillars of the Carina Nebula and the massive (5000 solar masses) Chameleon that is only 160-180 pc away from the Sun [13].

6 Galaxy Arm Information to Search for Continuous Gravitational Wave Sources

Another method was explored regarding where to look for potential sources of continuous gravitational waves: the spiral arms of the Milky Way Galaxy. The Milky Way Galaxy, in its more accepted form, has $m=4$ arms, a pitch angle of 12.8 degrees, a center located at (0 kpc, 0 kpc), and the Sun at the position (0 kpc, 7.6 kpc) [16]. Using information and data from [16, 17, 18], we made a model of the galaxy by reconstructing the spiral arms of the Milky Way Galaxy on [10] and plotting the position of the Sun. Following this, we computed the tangents to the spiral arms and plotted the corresponding tangent lines to the Sun on our model. Using information gathered from these lines, we then determined what we might see if we were to perform a search along these tangent lines.

6.1 Construction of a Model of the Milky Way Galaxy

The Milky Way Galaxy has $m=4$ spiral arms that are logarithmic spirals described by the equations [18]:

$$\begin{aligned} x &= r \cos(\theta) \\ y &= r \sin(\theta) \\ r &= r_0 e^{kz} \end{aligned} \quad (15)$$

where $r_0=2.1$, $z=(\theta - \theta_0) > 0$, $k=\tan(p)$, $p=12.8$ (pitch angle) and θ_0 is a constant that depends on the arm [18]. The Norma spiral arm has $\theta_0 = \frac{-20\pi}{180}$ [16]. To determine θ_0 for each of the other spiral arms: Norma-Cynius, Crux-Scutum, Carina-Sagittarius, and Perseus, one adds $\frac{\pi}{2}$ to the arm preceding it. Thus, for Norma-Cynius, $\theta_0 = \frac{-110\pi}{180}$, for Crux-Scutum $\theta_0 = \frac{-110\pi}{180}$, for Carina-Sagittarius $\theta_0 = \frac{-200\pi}{180}$, and for Perseus $\theta_0 = \frac{-290\pi}{180}$.

These spiral arms and the position of the Sun were then plotted. Afterwards, we plotted the tangent lines from the Sun to the spiral arms. To do this, we take the derivative of x and y from (15) with respect to θ :

$$\begin{aligned} \dot{x} &= r_0 e^{k(\theta-\theta_0)} \cos(\theta)k - r_0 e^{k(\theta-\theta_0)} \sin(\theta) \\ \dot{y} &= r_0 e^{k(\theta-\theta_0)} \sin(\theta)k + r_0 e^{k(\theta-\theta_0)} \cos(\theta) \end{aligned} \quad (16)$$

which simplifies to

$$v = r_0 e^{kz} \langle k \cos(\theta) - \sin(\theta), k \sin(\theta) + \cos(\theta) \rangle \quad (17)$$

where v is our tangent vector. We then convert to polar coordinates where we let

$$\begin{aligned} r &= \sqrt{k^2 + 1} \\ \varphi &= \frac{1}{\sqrt{k^2 + 1}} \end{aligned} \quad (18)$$

where we have a right triangle with a hypotenuse r , a height of 1, and $x=k$. Using the fact that $x = r \cos(\theta)$ and $y = r \sin(\theta)$, we can see that $k = r \cos(\theta)$ and that $1 = r \sin(\theta)$, which means that

$$\begin{aligned} k &= \sqrt{k^2 + 1} \cos(\varphi) \\ 1 &= \sqrt{k^2 + 1} \sin(\varphi) \end{aligned} \quad (19)$$

Substituting this into equation (17) and using product-to-sum formulas, we get

$$v = r_0 e^{kz} \langle \cos(\varphi + \theta), \sin(\varphi + \theta) \rangle \quad (20)$$

We are able to define φ by noting that in our right triangle

$$\tan(\varphi) = \frac{1}{k} \quad (21)$$

which means that φ and the pitch angle p are compliments of each other by the relationship

$$\frac{1}{\tan(\varphi)} = k = \tan(p). \quad (22)$$

Thus, $p = \frac{77.2\pi}{180}$.

We can then find the slope of our tangent line, which is

$$\frac{\dot{y}}{\dot{x}} = \frac{\sin(\varphi + \theta)}{\cos(\varphi + \theta)} \quad (23)$$

Using this slope, we can define the equations of our tangent lines as

$$y = \frac{\sin(\varphi + \theta)}{\cos(\varphi + \theta)} (x - r_0 e^{kz} \cos(\theta)) + r_0 e^{kz} \sin(\theta) \quad (24)$$

Using [10], the model of the Milky Way Galaxy with tangents to the spiral arms from the Sun was produced by choosing an accurate θ . The model is seen in Figure 16.

We then found the distance to each tangent from the sun and right ascension and declination of each tangent relative to the sun. To find the distance from the Sun, we simply use the equation

$$d = \sqrt{(x_{Sun} + r_0 e^{kz} \cos(\theta))^2 + (y_{Sun} - r_0 e^{kz} \sin(\theta))^2} \quad (25)$$

To find the right ascension and declination of each tangent line, we use the following equations provided by page 34 of [19] which allows from us to convert to equatorial coordinates (α, δ) from galactic coordinates (l, b)

$$\begin{aligned} \delta &= \arcsin(\cos(b) \cos(27.4) \sin(l - 33) + \sin(b) \sin(27.4)) \\ \alpha &= \arctan\left(\frac{\cos(b) \cos(l - 33)}{\sin(b) \cos(27.4) - \cos(b) \sin(27.4) \sin(l - 33)}\right) + 192.25 \end{aligned} \quad (26)$$

where b = galactic longitude, l = galactic latitude, α =right ascension, and δ =declination [19]. For us, the galactic longitude, $b=0$, and galactic latitude, l is our angle θ from $z=(\theta - \theta_0)$ used to find the tangent lines.

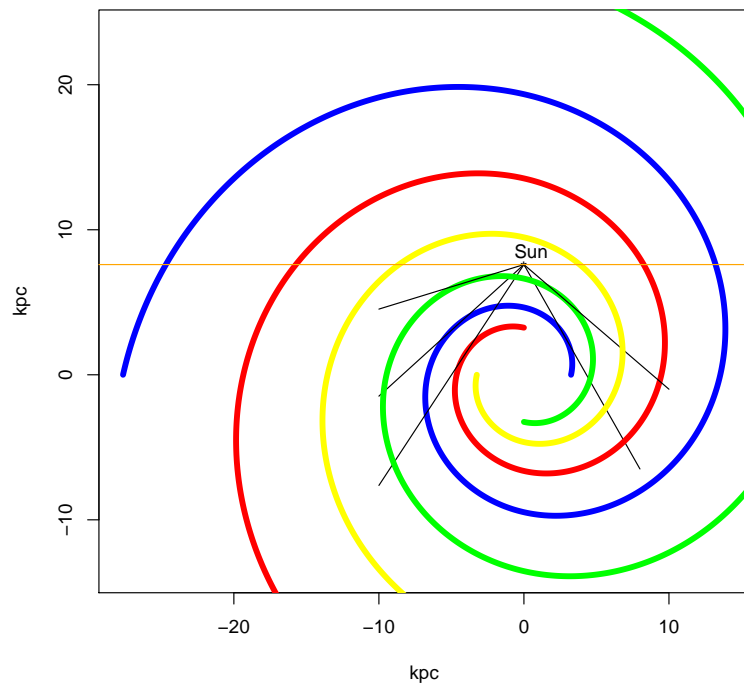


Figure 16: Plot of the Milky Way Galaxy's spiral arms and the tangent lines to these arms from the Sun.

| Arm | Degrees | Converted Degrees | Vallee | Distance to Sun(kpc) | RA | DEC |
|--------------------|---------|-------------------|--------|----------------------|------|--------|
| Carina-Sagittarius | 120 | 287.2 | 283 | 3.9 | 2.80 | -1.03 |
| Sagittarius-Carina | 61.962 | 49.162 | 52 | 3.7 | 1.92 | 0.25 |
| Crux-Scutum | 145.021 | 312.221 | 309 | 6.4 | 3.70 | -1.07 |
| Scutum-Crux | 42.403 | 29.603 | 31 | 5.8 | 4.90 | -0.052 |
| Norma-3kpc | 159.518 | 326.718 | 328 | 7.3 | 4.12 | -0.95 |

Table 6: Table of our data that we used to make and analyze the tangents to the spiral arms of the Milky Way Galaxy. The Perseus arm is not included as it is too close to the galactic center to be of any interest for a PowerFlux search. The column “Degrees” are the values we used of θ when making the tangent lines. The column “Converted Degrees” are the values we used to compare our results to those in [16]. [16] had used values relative to the galactic center. In order for us to make a comparison, we had to use the equation, $\theta + \phi \pm 90$. 90 degrees was added if the tangent line was in the second quadrant, 90 degrees was subtracted if tangent was in the first quadrant. “Vallee” are the degrees we are making a comparison to. As can be seen, our results are very close to our comparison and thus accurate. Due to its relatively small distance away from Earth and its position, the Carina-Sagittarius tangent would be ideal for a search. Other searches will be made as well for on the Sagittarius-Carina, Crux-Scutum, and Scutum-Crux. Norma may be too far away for a PowerFlux search.

Our results are summarized in Table 6, where we compare our angles used to make the tangent lines to those in [16].

Using this data, the SkyView Virtual Observatory [20] was used to see what we would find at locations that are close enough for us to perform a search using PowerFlux. What we found is seen in Figure 17.

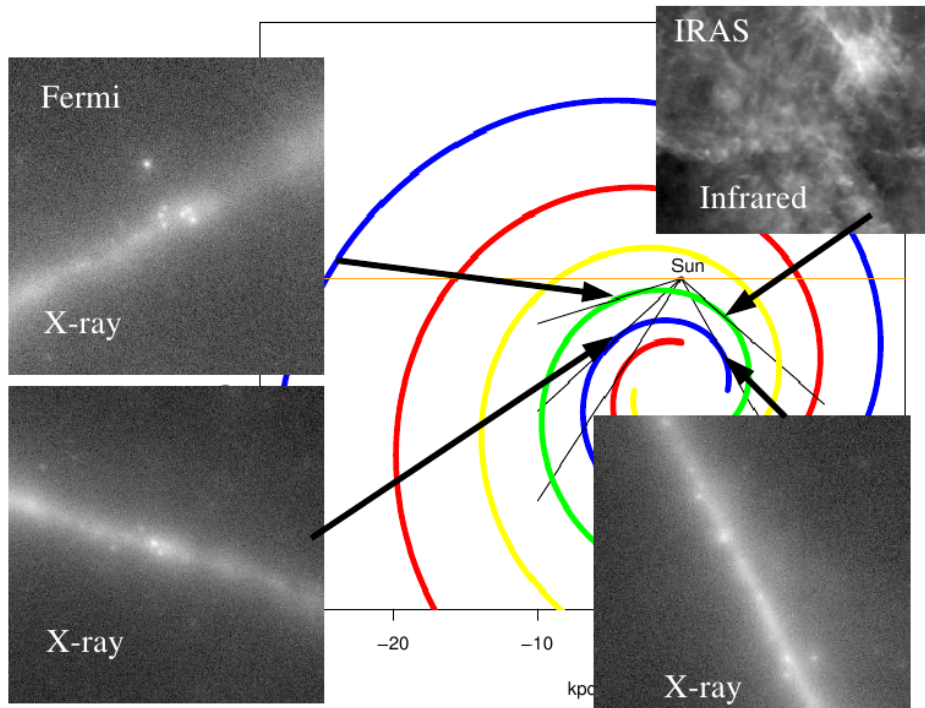


Figure 17: X-ray or Infrared emissions at the tangents of the spiral arms of the Milky Way Galaxy from either the FERMI or IRAS NAS mission [20].

Using the fact that we also know that the intensity of the Far Infrared Cooling lines peak along the tangents of the Spiral Arms of the Milky Way Galaxy, as seen in Figure 18 [16], we can conclude that searches of these locations for potential sources of CWs is worth our time.

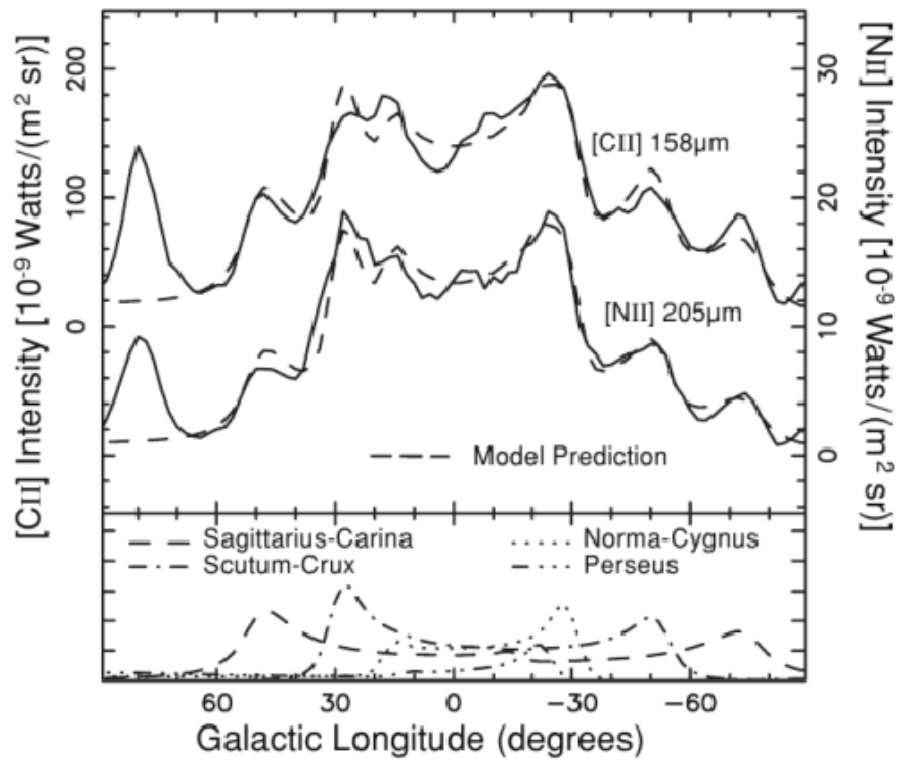


Figure 18: The Far Infrared Red Cooling Lines peak along the tangents of the Milky Way Galaxy, as indicated by this figure. Source: [16].

6.2 Search Space and Efficiency

We now explain how we determined the search space and efficiency of searches along the tangent lines to the Carina-Sagittarius arm. First, we fit a circle to the point of tangency. To do this, we used the basic equation of a circle $(x - a)^2 + (y - b)^2 = R^2$. Since a circle is defined by 3 points, we let one point of the circle be the point of tangency, and have the other two points defined by equation (15) that are varied until a proper circular fit is made. Since a circle is defined by $(x - a)^2 + (y - b)^2 = R^2$, which, through expansion, is $a^2 + b^2 + 2ax + 2by + z = 0$ (where $R = \sqrt{a^2 + b^2 - c}$) we must find the coefficients of our circle by solving the following system of equations:

$$\begin{aligned} 2a_1x + 2b_1y + z &= -(a_1^2 + b_1^2) \\ 2a_2x + 2b_2y + z &= -(a_2^2 + b_2^2) \\ 2a_3x + 2b_3y + z &= -(a_3^2 + b_3^2) \end{aligned} \quad (27)$$

where each equation is with respect to one of the three defined points of our circle explained above. This system was solved using [10] for each tangent to the Carina-Sagittarius arm, and the circles constructed.

If we draw a line at an angle α from the sun that intersect this circle at two points and rotate this line about the tangent line, we have a cone that we may use as our search space. The cone will have a volume of

$$V = \frac{\pi}{3}(h_1^3 - h_2^3)(\tan(\alpha))^2 \quad (28)$$

One then solves for the intersection of the circle, where the equation of the circle and the line in this case, are defined respectively as

$$\begin{aligned} x^2 - 2xd + d^2 + y^2 - 2yr - R^2 &= R^2 \\ y &= \tan(2\alpha)x \end{aligned} \quad (29)$$

This becomes the quadratic

$$x^2(\sec(\alpha))^2 - 2x(d + \tan(2\alpha)R) + d^2 = 0 \quad (30)$$

Using [10], we can solve this quadratic and find our search space with respect to alpha. The search space is graphically represented in Figure 19.

The efficiency of this search is graphically represented in Figure 20.

Similar analysis needs to be done for the other side of the Carina-Sagittarius arm and both sides of the Crux-Scutum arm.

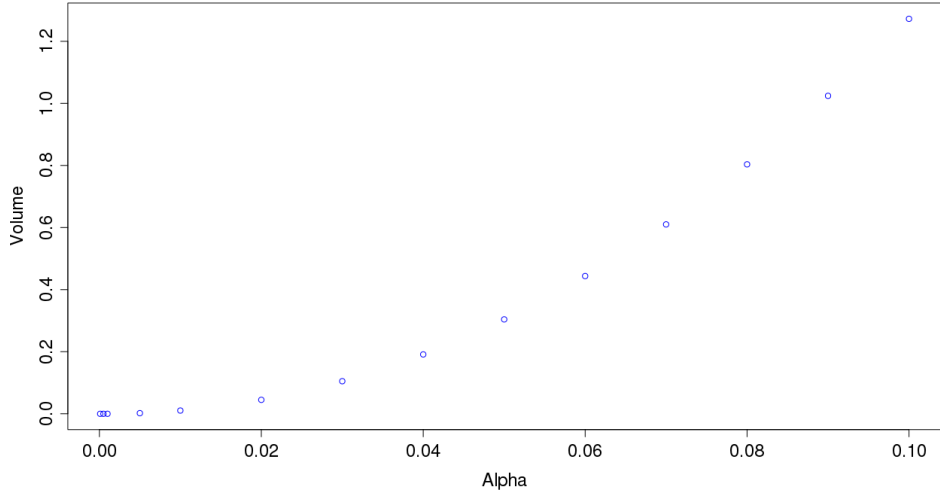


Figure 19: Volume of search space as alpha increases for the Carina-Sagittarius tangent line. The Volume is in units of kpc^3 .

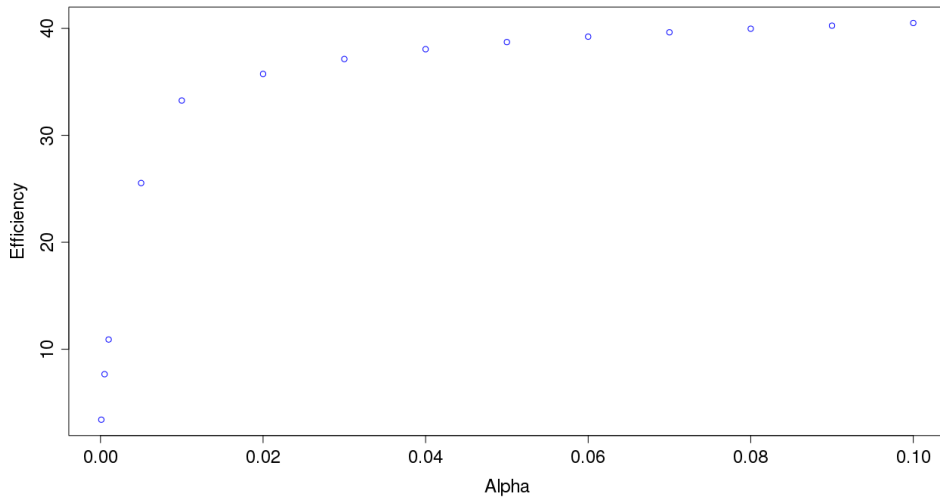


Figure 20: Efficiency of the Carina-Sagittarius tangent line search. The efficiency is in units of $\frac{kpc^3}{rad}$. The efficiency rapidly increases until the angle of ~ 0.02 radians.

7 Conclusions and Future Work

It was seen that as the speed of a gravitational wave varies, the reconstructed signal approaches the ecliptic pole to compensate for the greater Doppler effect from Earth when the speed of a gravitational wave is injected at less than the speed of light and away from the ecliptic pole when the speed of the injected signal is greater than the speed of light. The results of how PowerFlux responds to an 8 month and 16 month period during follow-up runs were discussed, and why certain chunks of data produce stronger signals. The next step is to run simulations of hundreds of injections of the 8 month and 16 month run and determine how well PowerFlux reconstructs parameters and is able to run follow-up runs on potential candidates. We have also successfully located some locations to search for sources of continuous gravitational waves. It was also seen that searching along the tangent lines of the Milky Way Galaxy will be useful in our search for these potential sources.

Future work consists of continuing analysis of S6 data outliers and determining the search space and efficiency for the Sagittarius side of the Carina-Sagittarius spiral arm and both sides of the Crux-Scutum spiral arm and performing these searches. Also, search spaces and efficiencies that are slightly off center from the tangent lines of the spiral arms will be determined.

References

- [1] B.P., Abbott, et al, *LIGO: the Laser Interferometer Gravitational Wave Observatory*, Rep. Prog. Phys. 72 076901, 2009.
- [2] Weinstein, Alan, *Introduction to Gravitational Waves and LIGO*, LIGO SURF Introductory Talk, 2006.
- [3] Sigg, Daniel, *Gravitational Waves*, LIGO Document, P980007-00 D, 1998.
- [4] Dergachev, Vladimir, *An all-sky search for continuous gravitational waves*, 2009.
- [5] Dergachev, Vladimir, *On blind searches for noise dominated signals: a loosely coherent approach*, 2011.

- [6] Dergachev, Vladimir, *Robustness of Broadband Searches for Continuous-Wave Gravitation Radiation to Deviations from Ideal Signal Model*, 2010.
- [7] Dergachev, Vladimir, *Broadband Search for Continuous-Wave Gravitation Radiation with LIGO*, LIGO Document, G1100002-v7, 2011.
- [8] Dergachev, Vladimir, *Description of PowerFlux 2 algorithms and implementation (draft)*, LIGO Document, LIGO-T1000272-v5, 2011.
- [9] WEBDA database, <http://www.univie.ac.at/webda/>.
- [10] R statistical analysis software, <http://www.r-project.org/>.
- [11] *Sights Within Our Galaxy*, 09 Aug. 2011 <http://www.cosmiclight.com/imagegalleries/ourgalaxy.htm>.
- [12] Smith, Nathan, Brooks, J. Kate, “The Carina Nebula: A Laboratory for Feedback and Triggered Star Formation.” *Handbook of Star Forming Regions Vol. II* Astronomical Society of the Pacific. Ed Bo Reipurth, 2008. 138-169.
- [13] Luhman, K.L., “Chamaeleon.” *Handbook of Star Forming Regions Vol. II* Astronomical Society of the Pacific. Ed Bo Reipurth, 2008.
- [14] ATNF pulsar database, <http://www.atnf.csiro.au/research/pulsar/psrcat/>
- [15] Hessels, Jason W. T., Ransom, Scott M., Stairs, Ingrid H., Freire, Paulo C. C., Kaspi, Victoria M., Camilo Fernando, *A Radio Pulsar Spinning at 716 Hz*, 2006.
- [16] Vallee, Jacques P., *New Velocitmetry and Revised Cartography of the Spiral Arms in the Milky Way—A Consistent Symbiosis*, 2008.
- [17] Vallee, Jacques P., *The Milky Way’s Spiral Arms Traced by Magnetic Fields, Dust, Gas, and Stars*, 1995.
- [18] Vallee, Jacques P., *METASTUDY OF THE SPIRAL STRUCTURE OF OUR HOME GALAXY*, 2001.

- [19] Duffett-Smith, Peter, *Practical Astronomy With Your Calculator*, Cambridge University Press, Cambridge, 1979.
- [20] Skyview database <http://skyview.gsfc.nasa.gov/>